

# Silica Shell Growth on Vitreophobic Gold Nanoparticles Probed by Plasmon Resonance Dynamics

Christian Engelbrekt,\* Yash Gargasya, and Matt Law\*



Cite This: <https://doi.org/10.1021/acs.jpcc.1c07969>



Read Online

ACCESS |



Metrics & More

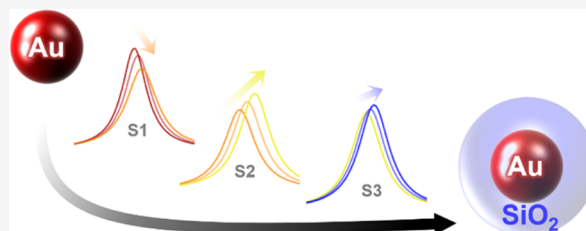


Article Recommendations



Supporting Information

**ABSTRACT:** The early stages of silica deposition on vitreophobic citrate-capped gold nanoparticles (AuNPs) are studied using *in situ* optical spectroscopy supported by electron microscopy and hydrodynamic size measurements. Through extinction spectra fitting, the time dependence of the surface plasmon resonance, which acts as a sensitive probe of the local environment, reveals three distinct stages of uniform silica shell formation on AuNPs. The first stage, which has not previously been reported, is characterized by an increase in plasmon damping by adsorption of silica precursors. The initial silica growth is shown by electron microscopy to be highly anisotropic, proceeding radially from the vertices of the faceted AuNPs before forming conformal shells.



## INTRODUCTION

Gold nanoparticles (AuNPs) have found application in areas as diverse as heterogeneous catalysis<sup>1,2</sup> and nanomedicine.<sup>3</sup> The excitation of collective oscillations of conduction electrons (plasmons) in gold nanomaterials, known as localized surface plasmon resonances (LSPRs), gives rise to strong, localized electromagnetic fields that enhance optical signals<sup>4</sup> from the visible to the infrared spectral range<sup>5,6</sup> and ultimately couples to phonons that heat the lattice and solvent.<sup>7,8</sup> The ability to sustain bright LSPR modes combined with excellent biocompatibility,<sup>9</sup> resistance to photobleaching,<sup>10</sup> chemical inertness, ease of preparation, and high X-ray contrast<sup>11</sup> make gold nanostructures versatile surface-enhanced Raman spectroscopy (SERS) probes and theranostic agents.<sup>4,11,12</sup>

Colloidal instability is detrimental to the function of AuNP sols in many applications.<sup>11,13</sup> The dispersed AuNPs aggregate when the stabilizing layer of organic ligands on the Au surface degrades, the Au–ligand interaction is disrupted, or the stabilizing electrostatic charge is screened, ultimately leading to sedimentation. It is challenging to avoid all of these possibilities during catalytic operation, under harsh conditions, or in complex biological environments.<sup>11</sup> However, coating the AuNPs with robust inorganic shells (*e.g.*, silica) has been very successful for synthesizing active and stable gold nanomaterials.<sup>14</sup> Silica is chosen because it is non-toxic, inert, hydrophilic, and cheap and because good control of silica sphere/shell growth has been achieved.<sup>14</sup> Furthermore, the silica shell acts as a physical spacer between the metal surface and the environment, which is essential for photonic crystals, where the metal spheres cannot be in direct contact,<sup>15–18</sup> and for fluorescence enhancement, where dye fluorescence is quenched at very small dye-metal distances.<sup>10,14,17,19,20</sup>

Nanotechnology based on colloidal silica started in 1968 with the work of Stöber, Fink, and Bohn, who presented a protocol for controllable synthesis of silica sols now known as the Stöber method.<sup>21</sup> Three decades later, Mulvaney, Giersig, and Liz-Marzán demonstrated silica growth on gold colloids *via* a modification of the Stöber method.<sup>22</sup> The process entailed three separate steps: (1) ligand exchange from citrate to aminosilane, (2) slow formation of a thin silica shell from active silica in water, and (3) further growth *via* alkoxysilane hydrolysis and condensation in ethanol. It was argued that the vitreophobic character of the citrate-terminated AuNP surface prevents the formation of conformal silica shells, prompting the replacement of citrate with aminosilane to provide a vitreophilic surface.<sup>22</sup> This report laid the foundation for the field of gold-silica core-shell nanoparticle (Au@SiO<sub>2</sub> NP) synthesis and applications. Since 1996, a number of modifications to the original report have been developed. The group of Xia directly coated commercial AuNPs with silica, omitting the two first steps of the previous protocol.<sup>18</sup> The Xia method, in which tetraethyl orthosilicate (TEOS) is hydrolyzed in a mixture of isopropyl alcohol (IPA) and water using ammonia as a catalyst, is frequently used for Au@SiO<sub>2</sub> NP synthesis. Many variations on these previous methods have been developed for various systems, and all consist of the same general components, that is, a silica precursor (sodium

**Received:** September 9, 2021

**Revised:** October 17, 2021

silicate,<sup>22–25</sup> tetra-methyl,<sup>23</sup> -ethyl<sup>10,11,13,17,18,22,24,26–34</sup> or -propyl<sup>23</sup> orthosilicate, or diglyceroxysilane<sup>32</sup>), a water/organic solvent mixture (ethanol,<sup>10,11,13,22–24,27–33</sup> methanol,<sup>23</sup> or IPA<sup>17,18,34</sup>), and base (NaOH<sup>11,23,26,29,31</sup> or NH<sub>4</sub>OH<sup>10,13,22,27,32–34</sup>). AuNPs of different shape and surface functionalization have been coated with silica. Commonly, silica shells are formed directly on spherical citrate-capped AuNPs (cit-AuNPs)<sup>10,13,18,27,33,34</sup> or after exchange of the original ligand with vitreophilic ligands such as (3-amino-propyl)-<sup>11,22,23</sup> or (3-mercaptopropyl)-trimethoxysilane<sup>23</sup> (APTMS or MPTMS) or polymers such as polyvinylpyrrolidone.<sup>10,28,32</sup>

The optical properties depend strongly on the thickness and morphology of the silica shell, and significant efforts have been made on understanding these relations.<sup>17,18</sup> Control of shell thickness is commonly achieved by varying the synthesis conditions (e.g., reactant concentrations, pH, and time), and subsequently, the optical properties of the final product are characterized.<sup>10,11,13,17,18,27,35</sup> Typically, the thinnest silica shells studied are >5 nm, and the dependence of the optical properties on silica shell thickness is similar across different studies: (i) the LSPR first redshifts and grows in intensity upon formation of a silica shell, (ii) this continues with increasing shell thickness until thick shells are formed, at which point (iii) an apparent blueshift ensues as scattering by the silica starts to dominate the spectrum.<sup>22</sup> Since most reports characterize only the final product, the early stages of silica shell formation, and therefore the very thin shells, are largely unexplored, despite the fact that Au@SiO<sub>2</sub> NPs with thin shells are especially important for SERS and catalysis applications. The Raman enhancement factor rapidly decays within a few nanometer of the surface, limiting the range for a beneficial combination of SERS and silica protection to thin silica shells.<sup>36,37</sup> Similarly, the application of shell-protected AuNPs for photothermal treatment may be compromised by thick, thermally insulating silica shells.<sup>37</sup>

There have been a few reports on the mechanism of silica deposition on colloidal AuNPs.<sup>33,34</sup> To the best of our knowledge, only one paper reports the time dependence of this process, and with relatively low time resolution (1 h).<sup>33</sup> Here, we employ time-resolved ultraviolet–visible (UV–vis) spectroscopy to monitor the formation of silica shells on AuNPs with ~1.5 min time resolution. By applying a simple analytical model to the spectra, the time dependence of the physically-motivated parameters describing the LSPR and the bulk silica can be extracted. The silica shell formation mechanism is studied through analysis of the formation kinetics under different reaction conditions. This analysis is supported by dynamic light scattering and *ex situ* electron microscopy imaging of Au@SiO<sub>2</sub> NPs at different stages of silica growth. The combination of high time resolution and the analytical model is crucial for the kinetic analysis that identifies a surface reaction preceding the formation of silica which may be rate limiting for shell formation. The early growth of silica is also shown to be non-uniform, with initial nucleation and growth on vertices/edges, and growth to several nanometers in thickness before coalescing into a conformal shell. This observation stresses the need for chemical surface modification on vitreophobic AuNPs to achieve uniform thin silica shell coatings.

Our approach further demonstrates how *in situ* UV–vis absorption spectroscopy and LSPR analysis can be used to obtain detailed kinetics information about chemical reactions

on colloidal AuNP surfaces. This approach can be applied broadly and may enable better synthesis control of composite AuNP-based nanomaterials.

## METHODS

**Chemicals.** HAuCl<sub>4</sub>·3H<sub>2</sub>O (Aldrich, ≥99.9%), trisodium citrate (TSC, MP Biomedicals, LLC, 99.8%), 2-propanol (IPA, Fischer Scientific, HPLC grade), TEOS (Aldrich, 99.999%), and 28–30% NH<sub>4</sub>OH in water (Fischer Chemicals) were used as received. Ultrapure water (18.2 MΩ) was obtained from a Milli-Q system from Millipore.

**AuNP Synthesis.** Synthesis of spheroidal AuNPs with controlled size was based on the protocol by Bastús *et al.*<sup>6</sup> First, AuNP seeds were prepared by injection, and subsequent reduction, of aqueous HAuCl<sub>4</sub> into TSC solution with final concentrations of 165 μM and 2.2 mM, respectively, at 95–100 °C and heating for 25 min. Then, a seeded-growth process was undertaken by sequentially injecting HAuCl<sub>4</sub>, removing a fraction of the growth solution after three HAuCl<sub>4</sub> injections, and adding more TSC solution. This produced a series of fractions of AuNPs of increasing size, Figure S1. A fraction consisting of 36 ± 9 nm AuNPs was used for the present study.

**Au@SiO<sub>2</sub> NP Synthesis.** For a 6 mL total volume of Au@SiO<sub>2</sub> sol prepared with 10 mM of TEOS, 0.7 mL of ultrapure water was added to 1 mL of AuNPs under stirring, followed by 4.1 mL of IPA and 150 μL of 14.5 M NH<sub>4</sub>OH (28% ammonia water). After mixing for 2–5 min, 60 μL of 1 M TEOS (in IPA) was injected. To adjust the TEOS concentration, the added volume of 1 M TEOS was modified, and that of IPA adjusted to compensate. Au@SiO<sub>2</sub> NP formation was performed at room temperature (r.t., 20 ± 1 °C) unless otherwise stated. Representative transmission electron microscopy (TEM) samples at given reaction times were obtained by quenching the reaction by extracting 100 μL of the reaction mixture and injecting it into an Eppendorf tube with 1–1.5 mL of water. The colloid was sedimented by centrifugation (16k rcf, 15 min), the supernatant reaction mixture was discarded, and the colloids redispersed in ultrapure water, which was then dropcast onto a TEM grid. For Au@SiO<sub>2</sub> NP synthesis in complete darkness, the synthesis was carried out in a dark laboratory in a foil-wrapped vial. Fractions were extracted into Al foil-wrapped Eppendorf tubes, and the TEM samples were covered while drying to exclude light.

**Characterization.** UV–vis extinction spectroscopy was carried out using a LAMBDA 950 spectrophotometer from PerkinElmer. For *in situ* spectroscopy, AuNP sol, ultrapure water, IPA, and NH<sub>4</sub>OH were mixed in this order in a glass vial with constant stirring to ensure quick mixing and avoid AuNP destabilization due to IPA and NH<sub>4</sub>OH addition. After stirring for 2–5 min, the desired amount of TEOS was added to the vial, the solution was quickly mixed with a pipette, poured into a glass cuvette, and then capped and immediately placed in the spectrometer, at which point continuous UV–vis measurements were initiated. The time delay between addition of TEOS and recording of the first spectrum was typically 10–20 s. For syntheses at controlled temperature, the sample cuvette was placed in a metal compartment cooled/heated by water from a circulating bath (Grand LT Ecocool 150), Figure S2.

TEM data were acquired on a JEOL 2800 microscope equipped with a 4k × 4k Gatan Oneview camera at 200 kV accelerating voltage at the Irvine Materials Research Institute, UC Irvine. Data were processed using ImageJ.<sup>38</sup>

*In situ* hydrodynamic size information was obtained with a Malvern Zetasizer Nano DLS instrument at the Laser Spectroscopy Labs, UC Irvine.

## RESULTS AND DISCUSSION

Silica shells were grown on AuNPs (Figures 1A and S1A) in an alkaline IPA–water mixture. A small volume of TEOS was

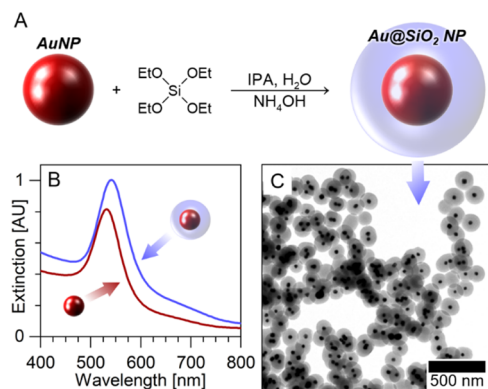


**Figure 1.** Preparation of Au@SiO<sub>2</sub> NPs. (A) Silica shells are formed around the cit-AuNPs from *via* TEOS hydrolysis and condensation. (B) Optical extinction spectra of the cit-AuNPs (green) and Au@SiO<sub>2</sub> NPs (blue). (C) Representative transmission electron micrograph of the final uniform core–shell product.

injected to initiate Au@SiO<sub>2</sub> NP formation, which was completed in 15 min to 2 h, depending on TEOS concentrations and temperature, Figure 1.

To monitor the Au@SiO<sub>2</sub> formation, UV–vis extinction spectra were continuously recorded while the shells grew on the colloidal AuNPs in a glass cuvette. A representative *in situ* spectral series (Figure 2A) shows three distinct stages of silica growth. The spectral changes during these stages are highlighted in Figure 2C–E. In the first stage, the LSPR

peak intensity and energy both decrease slightly (labeled red in the spectral series). In the second stage, a large and rapid increase in peak intensity occurs (labeled orange). The third stage is characterized by a slow increase in intensity across the entire spectrum (yellow and blue). We note that the initial drop in peak extinction has not been previously reported and may contain information about the early steps of silica shell formation.

To better understand the spectral behavior and derive its time dependence, a model of the extinction spectrum was applied. The *in situ* spectra were modeled with three contributions: the LSPR, the gold sp ← d interband transition, and scattering from the silica shell. These contributions are represented by a Lorentzian distribution, a logistic function (broadened step function), and an exponential growth function, respectively, as shown in eq 1

$$A(E) = \underbrace{\frac{1/2\pi c_p \cdot \gamma_p}{(E - E_p)^2 + \left(\frac{\gamma_p}{2}\right)^2}}_{\text{plasmon}} + \underbrace{\frac{c_i}{1 + e^{-(E - E_i/\gamma_i)}}}_{\text{interband}} + \underbrace{c_s(e^{b_s E} - \gamma_s)}_{\text{silica}} \quad (1)$$

The parameters for the interband transition, that is,  $c_i$ ,  $\gamma_i$ , and  $E_i$ , are determined by fitting the first spectrum, where silica has not yet formed and does not contribute. These parameters are then fixed for all the following spectra in an experiment. Similarly, the shape of the silica contribution is determined by fitting spectra of silica particle formation in the absence of AuNPs (Figure S3). Here, the spectrum is solely determined by the silica contribution and found to be well represented by an exponential growth function (extinction *vs* energy). The shape of the silica extinction spectrum (represented by the parameters  $b_s$  and  $\gamma_s$ ) did not change during silica growth, so these parameters were fixed in the fits of silica growth on the

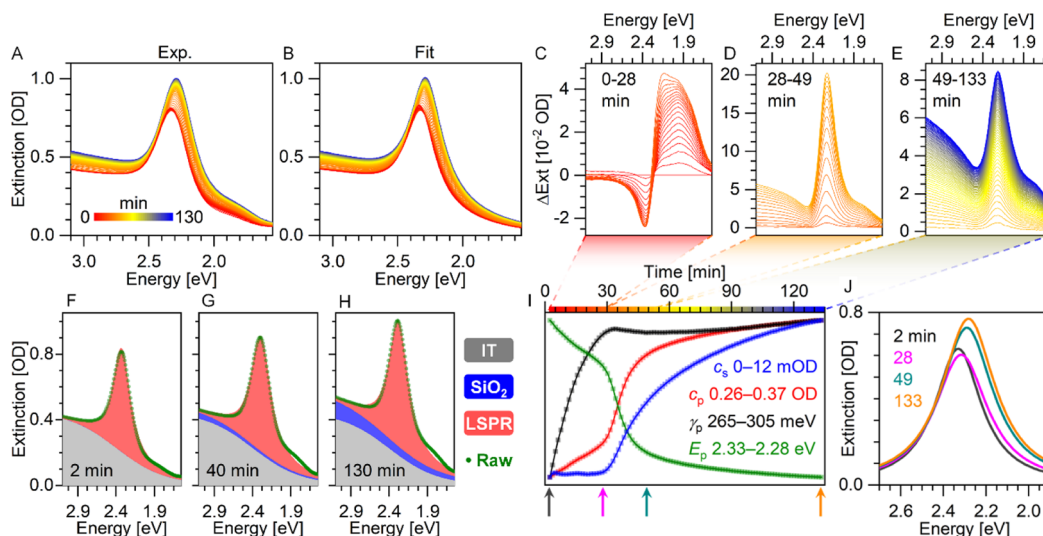


**Figure 2.** Analysis of *in situ* UV–vis spectra shown for standard reaction conditions ( $20 \pm 1$  °C, 2 mM TEOS). (A) Experimental and (B) fitted *in situ* spectra. (C–E) Difference spectra showing the change occurring in each distinct stage. (F–H) Recorded spectra (green symbols) and contributions from the interband transition (gray shading), LSPR (red shading), and SiO<sub>2</sub> (blue shading) at three different times during reaction. (I) Time dependence of the fitting parameters. The color scale on the *x*-axis correlates to the color scheme of the spectra in (A–E). The *y*-axis values are different for each fitting parameter (see the legend). (J) LSPR spectra extracted from fits of the first spectrum (gray) and the spectra at the end of each stage. The corresponding time points are indicated with colored arrows in (I).

AuNPs. Overall, there are four time-dependent parameters to be extracted from each spectrum, namely, the three parameters for the plasmon ( $c_p$ ,  $\gamma_p$ , and  $E_p$ ) and one for the scattering intensity (amount) of the silica ( $c_s$ ). As seen in Figures 2A,B and S4, this model very accurately reproduces the experimental data except for the weak shoulder at  $\sim 1.8$  eV that is related to a small amount of aggregation induced by the change in the AuNP environment upon addition of IPA and  $\text{NH}_4\text{OH}$ . The aggregation process was effectively instantaneous and had completed before the addition of TEOS, so it did not contribute to the dynamics of silica formation. The accuracy of the fitting model and the time dependence of the parameters were further tested by fitting a series of spectra calculated using Mie theory (Figure S5). The model reproduces the calculated spectra well and provides shell thickness-dependent parameters that agree well with time-dependent parameters extracted from fitting of the experimental spectra (Figure 2I).

Examples of deconvoluted *in situ* spectra are presented in Figure 2F–H, showing the LSPR on top of the interband transition to which a contribution from silica is added. Figure 2I shows the evolution of the four fitting parameters from eq 1 during a representative Au@SiO<sub>2</sub> NP synthesis with  $\sim 80$  s time resolution. Here, the three distinct stages are clearly observed. Stage 1 (S1) is dominated by plasmon broadening, stage 2 (S2) is dominated by rapid plasmon redshift and intensity increase, and stage 3 (S3) is dominated by a continuous increase in the silica contribution. The fits show that the decrease in LSPR peak intensity in S1 (Figure 2A) does not arise from a reduced intensity of the LSPR ( $c_p$  does not decrease) but rather from peak broadening and redshifting down the sloping interband transition (Figure 2J).

S2 and S3 correlate well with observations of LSPR dependence on silica thickness by Liz-Marzán and Mulvaney,<sup>22</sup> and others.<sup>11,13,18,27,35</sup> Initially, a redshift occurs followed by increased intensity. This can be explained by changes to the dielectric function of the medium,  $\epsilon_m$ , as the silica shell is growing and can be reproduced by Mie theory (as seen in Figure S5 and shown previously<sup>22</sup>). Changes to  $\epsilon_m$  do not explain the behavior observed during S1, which has not yet been described in the literature.

In order to better understand the chemistry of S1–S3, the reaction kinetics were investigated by varying the TEOS concentration (1–15 mM) and reaction temperature (20–60 °C). The limits for these parameters were set by the stability of the AuNP sol. The time dependence of all parameters at all experimental conditions is given in Figures S6–S10. In Figure 3, the effect of reaction conditions on the evolution of the LSPR energy is represented by the  $E_p$  time curves and on the formation of silica by the  $c_s$  time curves. While these parameters do not have direct interpretations as concentrations of reactants or products, apparent process rates can be extracted from the time curves, and their dependence on experimental conditions is evaluated. The inverse sigmoidal shape of the  $E_p$  time curves can be viewed as three approximately linear segments with intersections that indicate the transitions between reaction stages, that is,  $t_1$  (S1  $\rightarrow$  S2) and  $t_2$  (S2  $\rightarrow$  S3). These transition times together with the maximum rate of the LSPR energy shift (middle of S2) can be conveniently extracted by fitting the first derivative of  $E_p(t)$  with a Gaussian function with full width at half-maximum,  $w$ , and center,  $t_{\text{max}}$ , as illustrated in Figure S11. An additional kinetic parameter describing S3 is taken as the maximum rate

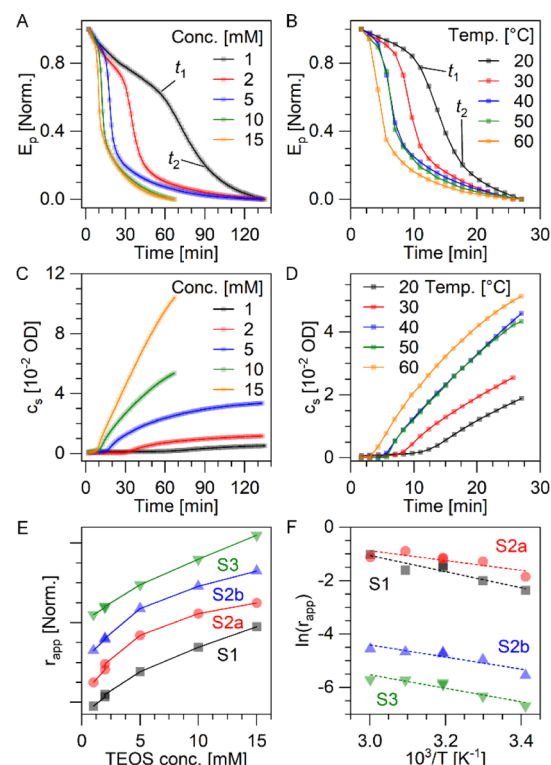


**Figure 3.** Kinetics analysis of Au@SiO<sub>2</sub> NP formation. (A,B) Normalized time-dependence of LSPR energy,  $E_p$ , (C,D) silica scattering intensity,  $c_s$ , and (E,F) kinetic parameters, at varying [TEOS] at r.t. (left column), and various reaction temperatures at 10 mM TEOS (right column). In (A,B), the transition times  $t_1$  and  $t_2$  are indicated with markers for the slowest reaction (black). In (E,F),  $r_{\text{app}}$  are determined by the duration of S1 (black), the duration of S2 (red), the max rate of change of S2 (blue), and the max rate of change of S3 (green).

of increase in silica scattering, that is, the maximum of the first derivative of the  $c_s$  time traces.

The four apparent rates,  $r_{\text{app}}$ , are thus defined as

$$\begin{aligned} r_{S1} &= t_1^{-1} = \frac{1}{t_{\text{max}} - 0.5w} \\ r_{S2a} &= t_2 - t_1 = \frac{1}{t_{\text{max}} + 0.5w} \\ r_{S2b} &= \max \left| dE_p / dt \right| \\ r_{S3} &= \max |dc_s / dt| \end{aligned} \quad (2)$$

These four kinetic parameters can be considered as apparent rates for S1, S2, and S3, that is, the inverse of the duration of S1 and S2 and the maximum rates of change for S2 and S3. Plotting the rates against the TEOS concentration provides insights into the reaction order, Figure 3E. S1 and S3 display approximately linear dependence on the TEOS concentration, indicating that these processes are of first order in TEOS. However, the S2 (and to some extent S1) rates show a diminishing increase with increasing TEOS concentrations. This can be understood as S2 representing a surface reaction occurring on the AuNPs that is limited by the reactant concentration on the surface rather than that in solution. The reaction order thus approaches zero at high TEOS concentrations since the fixed number of surface sites on the

AuNPs are all occupied, and an increase in the TEOS concentration no longer leads to a rate increase. This surface reaction (S2) may be attributed to the formation of silica through condensation, as shown in Figure 1A, agreeing with the emergence of SiO<sub>2</sub> scattering in this phase. This further indicates that S1 describes a step that precedes silica formation, which may be the association of silica precursor species with the AuNP surface and formation of partly hydrolyzed/condensed pre-silica networks.

The rate dependence on temperature was studied in a similar fashion between 20 and 60 °C at a fixed TEOS concentration of 10 mM (right column in Figure 3). The Arrhenius-style plot in Figure 3F shows that the temperature dependence of the rates are slightly larger for S1 than S2 and S3. This is in good agreement with the generally accepted vitreophobic nature of citrate-stabilized AuNPs and the larger energy barrier associated with the adsorption of silica precursors on the citrate-terminated surface than with growth of the resulting vitreophilic silica shell. Our data thus indicate that the rate of Au@SiO<sub>2</sub> formation is limited by adsorption of molecular silica precursors and/or formation of pre-silica networks. The LSPR broadening of the colloid during S1 further support this interpretation, in agreement with previous reports showing a strong correlation between the LSPR width and the nature of the chemical interface at the surface of the plasmonic metal.<sup>39,40</sup> This mechanism of LSPR broadening was associated with both charge transfer to adsorbates and induction of surface dipoles.<sup>40</sup>

A comparison of the Au@SiO<sub>2</sub> NP morphology at different temperatures was made by quenching the silica formation reaction by 10-fold dilution in water after 30 min (Figure S12). At 20 °C, 30 min corresponds to the beginning of S3. These NPs showed only thin or partial SiO<sub>2</sub> shells. These shells provided insufficient stabilization, and the NPs had therefore aggregated during centrifugation. However, thick SiO<sub>2</sub> shells had formed after 30 min at 40 °C, where the reaction had progressed well into S3. These observations suggest that SiO<sub>2</sub> formation starts in S2 and continues through S3.

The correlation between optical properties and NP size/morphology was further verified by *in situ* monitoring of the hydrodynamic NP diameter and TEM imaging of quenched reaction products around the S2/S3 transition (Figures 4 and S14). The hydrodynamic diameter,  $d_h$ , does not change significantly during S1. In fact,  $d_h$  follows very closely the time curve of  $c_s$ , supporting the correlation between  $c_s$  and the growth of the SiO<sub>2</sub> shell. The quenched reaction products exhibited highly non-uniform SiO<sub>2</sub> shells at early reaction times. As the final Au@SiO<sub>2</sub> NPs appear nearly perfectly spherical, this was unexpected. The non-uniform growth was especially obvious on the small fraction of AuNPs that are anisotropic (e.g., truncated prisms), as seen in Figure 4B–F. During S2, SiO<sub>2</sub> forms in patches that are localized at AuNP vertices and edges, indicating that nucleation happens preferentially at sites of high local curvature. This may be due to curvature-dependent chemical properties of the ligand shell<sup>41</sup> or lower local ligand densities, which has been used in similar systems to selectively coat gold nanorod tips.<sup>31,42</sup> We note that SiO<sub>2</sub> nucleation in solution (rather than on the AuNP surface) followed by attachment to the NP surface is unlikely. First, empty SiO<sub>2</sub> particles in the final product are rare (~10%), and primary SiO<sub>2</sub> nuclei are only found associated with the AuNPs, and second, SiO<sub>2</sub> formation (the rise of  $c_s$ ) is

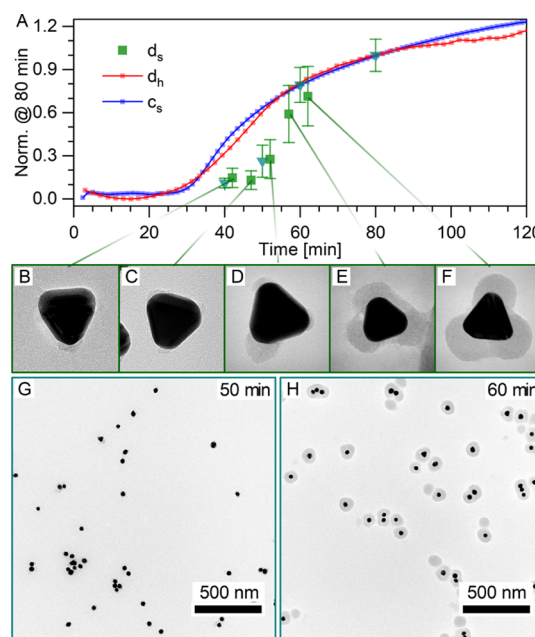


**Figure 4.** (A) Comparison of the time-dependence of silica shell thickness determined by TEM,  $d_s$  (symbols), hydrodynamic diameter,  $d_h$  (red), and the silica component from *in situ* spectra,  $c_s$  (blue). (B–F) TEM micrographs of individual-faceted AuNPs at different times of Au@SiO<sub>2</sub> formation in complete darkness (green squares in A). (G,H) TEM micrographs of fractions taken during an *in situ* spectroscopy experiment (cyan triangles in A). [TEOS] = 2 mM.

significantly slower in the absence of AuNPs, indicating the primarily heterogeneous SiO<sub>2</sub> nucleation on AuNP surfaces.

Through *in situ* UV–vis spectroscopy, we have identified three reaction stages in the formation of Au@SiO<sub>2</sub> NPs *via* SiO<sub>2</sub> growth on cit-AuNPs and associated them with distinct processes. S1 appears as an induction phase where no SiO<sub>2</sub> forms, but the sensitive LSPR probe reports significant changes on the AuNP surface. We assign the LSPR broadening to adsorption of silica precursor species on the citrate-terminated gold surface, such as orthosilicate anions, and formation of low-density pre-silica networks of partly condensed structures. This process is a prerequisite for shell formation and may influence the properties of the core–shell product, highlighting the importance of being able to probe this step and the merits of our approach. The subsequent condensation and densification, forming SiO<sub>2</sub> patches, change the dielectric function of the surroundings, causing the LSPR to redshift and intensify during S2, as has been reported previously.<sup>11,13,18,22,27,35</sup> This process is accelerated on vertices possibly because their lower density of citrate ligands facilitates the adsorption of SiO<sub>2</sub> precursor species. In the final stage (S3), the SiO<sub>2</sub> shell grows approximately isotropically until it terminates when the TEOS is consumed. The LSPR only changes slightly in this phase as further shell growth happens too far from the AuNP surface to affect the plasmon.

## CONCLUSIONS

We used *in situ* UV–vis spectroscopy to follow the formation of SiO<sub>2</sub> shells on 36 ± 9 nm citrate-capped AuNPs *via* a modified Stöber approach. This process combines the most widely used AuNPs with the most popular SiO<sub>2</sub> synthesis method. Despite being vitreophobic in nature, uniform SiO<sub>2</sub> shells successfully form directly on cit-AuNPs.

Using the LSPR to report on the surface processes, we have shown three distinct stages of Au@SiO<sub>2</sub> formation. (1) Adsorption of SiO<sub>2</sub> precursor species on the citrate-terminated gold surface causing broadening of the LSPR. (2) The formation of thin, discontinuous silica islands on the AuNP surface and thin SiO<sub>2</sub> shells, leading to LSPR redshifting and intensification. (3) Continued SiO<sub>2</sub> growth to produce a uniform SiO<sub>2</sub> shell increasing in thickness.

From the TEOS concentration and temperature dependence of the stages, the highest reaction barrier is associated with the adsorption of silica precursors (S1). S2 is associated with the condensation of SiO<sub>2</sub> precursor species to form SiO<sub>x</sub>. Finally, TEM studies of quenched reaction intermediates showed that nucleation of SiO<sub>2</sub> occurs preferentially on vertices of faceted/anisotropic AuNPs. These nuclei grow approximately isotropically rather than along the NP surface before ultimately coalescing into a uniform shell.

This study provides new details of SiO<sub>2</sub> formation on vitreophobic AuNPs and serves as an example of how *in situ* UV–vis spectroscopy and LSPR analysis can be utilized to obtain kinetic information of AuNP surface processes. Such studies can be widely applied and facilitate better synthesis control of Au@SiO<sub>2</sub> NPs and other multi-component nanomaterials, as well as providing insights into processes such as adsorption and surface functionalization.

## ■ ASSOCIATED CONTENT

### SI Supporting Information

The Supporting Information is available free of charge at <https://pubs.acs.org/doi/10.1021/acs.jpcc.1c07969>.

Experimental results including UV–vis spectroscopy and TEM data (PDF)

## ■ AUTHOR INFORMATION

### Corresponding Authors

Christian Engelbrekt – Department of Chemistry, University of California Irvine, Irvine, California 92697, United States; Department of Chemistry, Technical University of Denmark, Kongens Lyngby 2800, Denmark; [orcid.org/0000-0003-3679-3666](https://orcid.org/0000-0003-3679-3666); Email: [cheng@kemi.dtu.dk](mailto:cheng@kemi.dtu.dk)

Matt Law – Department of Chemistry, University of California Irvine, Irvine, California 92697, United States; [orcid.org/0000-0001-7645-9908](https://orcid.org/0000-0001-7645-9908); Email: [lawm@uci.edu](mailto:lawm@uci.edu)

### Author

Yash Gargasya – Department of Chemistry, University of California Irvine, Irvine, California 92697, United States; [orcid.org/0000-0003-0324-090X](https://orcid.org/0000-0003-0324-090X)

Complete contact information is available at: <https://pubs.acs.org/doi/10.1021/acs.jpcc.1c07969>

### Author Contributions

C.E. and M.L. designed the study. C.E. and Y.G. carried out synthesis and spectroscopy, and C.E. carried out TEM and DLS measurements. ML directed the study. All authors were involved with data analysis and contributed to the writing of the manuscript. All authors have given approval to the final version of the manuscript.

### Notes

The authors declare no competing financial interest.

## ■ ACKNOWLEDGMENTS

C.E. received financial support from the Independent Research Fund Denmark (DFF-5054-00107). Y.G. and M.L. were supported by the National Science Foundation (NSF) Center for Chemical Innovation on Chemistry at the Space-Time Limit (CaSTL), grant number CHE-1414466. TEM characterization was performed at the user facilities of the UC Irvine Materials Research Institute (IMRI), which is supported in part by the NSF through the UC Irvine Materials Research Science and Engineering Center (DMR-2011967). We thank the Laser Spectroscopy Labs at UC Irvine.

## ■ REFERENCES

- (1) Panigrahi, S.; Basu, S.; Praharaj, S.; Pande, S.; Jana, S.; Pal, A.; Ghosh, S. K.; Pal, T. Synthesis and Size-Selective Catalysis by Supported Gold Nanoparticles: Study on Heterogeneous and Homogeneous Catalytic Process. *J. Phys. Chem. C* **2007**, *111*, 4596–4605.
- (2) Ciriminna, R.; Falletta, E.; Della Pina, C.; Teles, J. H.; Pagliaro, M. Industrial Applications of Gold Catalysis. *Angew. Chem., Int. Ed.* **2016**, *55*, 14210–14217.
- (3) Dreaden, E. C.; Alkilany, A. M.; Huang, X.; Murphy, C. J.; El-Sayed, M. A. The Golden Age: Gold Nanoparticles for Biomedicine. *Chem. Soc. Rev.* **2012**, *41*, 2740.
- (4) Webb, J. A.; Bardhan, R. Emerging Advances in Nanomedicine with Engineered Gold Nanostructures. *Nanoscale* **2014**, *6*, 2502.
- (5) Jain, P. K.; Huang, X.; El-Sayed, I. H.; El-Sayed, M. A. Review of Some Interesting Surface Plasmon Resonance-Enhanced Properties of Noble Metal Nanoparticles and Their Applications to Biosystems. *Plasmonics* **2007**, *2*, 107–118.
- (6) Bastús, N. G.; Comenge, J.; Puentes, V. Kinetically Controlled Seeded Growth Synthesis of Citrate-Stabilized Gold Nanoparticles of up to 200 Nm: Size Focusing versus Ostwald Ripening. *Langmuir* **2011**, *27*, 11098–11105.
- (7) Hogan, N. J.; Urban, A. S.; Ayala-Orozco, C.; Pimpinelli, A.; Nordlander, P.; Halas, N. J. Nanoparticles Heat through Light Localization. *Nano Lett.* **2014**, *14*, 4640–4645.
- (8) Huang, X.; Jain, P. K.; El-Sayed, I. H.; El-Sayed, M. A. Plasmonic Photothermal Therapy (PPTT) Using Gold Nanoparticles. *Lasers Med. Sci.* **2008**, *23*, 217–228.
- (9) Moreira, A. F.; Rodrigues, C. F.; Reis, C. A.; Costa, E. C.; Correia, I. J. Gold-Core Silica Shell Nanoparticles Application in Imaging and Therapy: A Review. *Microporous Mesoporous Mater.* **2018**, *270*, 168–179.
- (10) Huang, Y.-F.; Ma, K.-H.; Kang, K.-B.; Zhao, M.; Zhang, Z.-L.; Liu, Y.-X.; Wen, T.; Wang, Q.; Qiu, W.-Y.; Qiu, D. Core–Shell Plasmonic Nanostructures to Fine-Tune Long Au Nanoparticle–Fluorophore Distance and Radiative Dynamics. *Colloids Surf., A* **2013**, *421*, 101–108.
- (11) Kobayashi, Y.; Inose, H.; Nakagawa, T.; Gonda, K.; Takeda, M.; Ohuchi, N.; Kasuya, A. Control of Shell Thickness in Silica-Coating of Au Nanoparticles and Their X-Ray Imaging Properties. *J. Colloid Interface Sci.* **2011**, *358*, 329–333.
- (12) Vo-Dinh, T.; Liu, Y.; Fales, A. M.; Ngo, H.; Wang, H. N.; Register, J. K.; Yuan, H.; Norton, S. J.; Griffin, G. D. SERS Nanosensors and Nanoreporters: Golden Opportunities in Biomedical Applications. *Wiley Interdiscip. Rev.: Nanomed. Nanobiotechnol.* **2015**, *7*, 17–33.
- (13) Mine, E.; Yamada, A.; Kobayashi, Y.; Konno, M.; Liz-Marzán, L. M. Direct Coating of Gold Nanoparticles with Silica by a Seeded Polymerization Technique. *J. Colloid Interface Sci.* **2003**, *264*, 385–390.
- (14) Hanske, C.; Sanz-Ortiz, M. N.; Liz-Marzán, L. M. Silica-Coated Plasmonic Metal Nanoparticles in Action. *Adv. Mater.* **2018**, *30*, 1707003.
- (15) Jain, P. K.; Lee, K. S.; El-sayed, I. H.; El-sayed, M. A. Calculated Absorption and Scattering Properties of Gold Nanoparticles of

Different Size, Shape, and Composition: Applications in Biological Imaging and Biomedicine. *J. Phys. Chem. B* **2006**, *110*, 7238–7248.

(16) Ung, T.; Liz-Marzán, L. M.; Mulvaney, P. Optical Properties of Thin Films of Au@SiO<sub>2</sub> Particles. *J. Phys. Chem. B* **2001**, *105*, 3441–3452.

(17) Rodríguez-Fernández, J.; Pastoriza-Santos, I.; Pérez-Juste, J.; García de Abajo, F. J.; Liz-Marzán, L. M. The Effect of Silica Coating on the Optical Response of Sub-Micrometer Gold Spheres. *J. Phys. Chem. C* **2007**, *111*, 13361–13366.

(18) Lu, Y.; Yin, Y.; Li, Z.-Y.; Xia, Y. Synthesis and Self-Assembly of Au@SiO<sub>2</sub> Core–Shell Colloids. *Nano Lett.* **2002**, *2*, 785–788.

(19) Dulkeith, E.; Ringler, M.; Klar, T. A.; Feldmann, J.; Muñoz Javier, A.; Parak, W. J. Gold Nanoparticles Quench Fluorescence by Phase Induced Radiative Rate Suppression. *Nano Lett.* **2005**, *5*, 585–589.

(20) Kim, C. K.; Kalluru, R. R.; Singh, J. P.; Fortner, A.; Griffin, J.; Darbha, G. K.; Ray, P. C. Gold-Nanoparticle-Based Miniaturized Laser-Induced Fluorescence Probe for Specific DNA Hybridization Detection: Studies on Size-Dependent Optical Properties. *Nanotechnology* **2006**, *17*, 3085–3093.

(21) Stöber, W.; Fink, A.; Bohn, E. Controlled Growth of Monodisperse Silica Spheres in the Micron Size Range. *J. Colloid Interface Sci.* **1968**, *26*, 62–69.

(22) Liz-Marzán, L. M.; Giersig, M.; Mulvaney, P. Synthesis of Nanosized Gold-Silica Core-Shell Particles. *Langmuir* **1996**, *12*, 4329–4335.

(23) Nooney, R. I.; Thirunavukkarasu, D.; Chen, Y.; Josephs, R.; Ostafin, A. E. Self-Assembly of Mesoporous Nanoscale Silica/Gold Composites. *Langmuir* **2003**, *19*, 7628–7637.

(24) Park, Y.-S.; Liz-Marzán, L. M.; Kasuya, A.; Kobayashi, Y.; Nagao, D.; Konno, M.; Mamykin, S.; Dmytruk, A.; Takeda, M.; Ohuchi, N. X-Ray Absorption of Gold Nanoparticles with Thin Silica Shell. *J. Nanosci. Nanotechnol.* **2006**, *6*, 3503–3506.

(25) Liz-Marzán, L. M.; Mulvaney, P. Au@SiO<sub>2</sub> Colloids: Effect of Temperature on the Surface Plasmon Absorption. *New J. Chem.* **1998**, *22*, 1285–1288.

(26) Gorelikov, I.; Matsuura, N. Single-Step Coating of Mesoporous Silica on Cetyltrimethyl Ammonium Bromide-Capped Nanoparticles. *Nano Lett.* **2008**, *8*, 369–373.

(27) Lee, H. B.; Yoo, Y. M.; Han, Y.-H. Characteristic Optical Properties and Synthesis of Gold-Silica Core-Shell Colloids. *Scr. Mater.* **2006**, *55*, 1127–1129.

(28) Zhao, Y.; Yang, D.; Hu, H.; Chen, L.; Xu, Y.; Qu, L.; Yang, P.; Zhang, Q. A Simple Approach to the Synthesis of Eccentric Au@SiO<sub>2</sub> Janus Nanostructures and Their Catalytic Applications. *Surf. Sci.* **2016**, *648*, 313–318.

(29) Wang, F.; Cheng, S.; Bao, Z.; Wang, J. Anisotropic Overgrowth of Metal Heterostructures Induced by a Site-Selective Silica Coating. *Angew. Chem., Int. Ed.* **2013**, *52*, 10344–10348.

(30) Meena, S. K.; Goldmann, C.; Nassoko, D.; Seydou, M.; Marchandier, T.; Moldovan, S.; Ersen, O.; Ribot, F.; Chanéac, C.; Sanchez, C.; et al. Nanophase Segregation of Self-Assembled Monolayers on Gold Nanoparticles. *ACS Nano* **2017**, *11*, 7371–7381.

(31) Hinman, J. G.; Eller, J. R.; Lin, W.; Li, J.; Li, J.; Murphy, C. J. Oxidation State of Capping Agent Affects Spatial Reactivity on Gold Nanorods. *J. Am. Chem. Soc.* **2017**, *139*, 9851–9854.

(32) Vanderkooy, A.; Chen, Y.; Gonzaga, F.; Brook, M. A. Silica Shell/Gold Core Nanoparticles: Correlating Shell Thickness with the Plasmonic Red Shift upon Aggregation. *ACS Appl. Mater. Interfaces* **2011**, *3*, 3942–3947.

(33) Qu, Q.; Liu, S. T. Coating Time Effect on Surface Structures of Silica-Encapsulated Gold Nanoparticles. *Adv. Mater. Res.* **2009**, *79–82*, 935–938.

(34) Ye, J.; Van de Broek, B.; De Palma, R.; Libaers, W.; Clays, K.; Van Roy, W.; Borghs, G.; Maes, G. Surface Morphology Changes on Silica-Coated Gold Colloids. *Colloids Surf., A* **2008**, *322*, 225–233.

(35) Kobayashi, Y.; Inose, H.; Nakagawa, T.; Gonda, K.; Takeda, M.; Ohuchi, N.; Kasuya, A. Synthesis of Au–Silica Core–Shell Particles by Sol–Gel Process. *Surf. Eng.* **2012**, *28*, 129–133.

(36) Stiles, P. L.; Dieringer, J. A.; Shah, N. C.; Van Duyne, R. P. Surface-Enhanced Raman Spectroscopy. *Annu. Rev. Anal. Chem.* **2008**, *1*, 601.

(37) Chen, M.; He, Y.; Zhu, J. Quantifying and Comparing the Near-Field Enhancement, Photothermal Conversion, and Local Heating Performance of Plasmonic SiO<sub>2</sub>@Au Core-Shell Nanoparticles. *Plasmonics* **2019**, *14*, 1019–1027.

(38) Schneider, C. A.; Rasband, W. S.; Eliceiri, K. W. NIH Image to ImageJ: 25 Years of Image Analysis. *Nat. Methods* **2012**, *9*, 671–675.

(39) Moon, S. W.; Tsalu, P. V.; Ha, J. W. Single Particle Study: Size and Chemical Effects on Plasmon Damping at the Interface between Adsorbate and Anisotropic Gold Nanorods. *Phys. Chem. Chem. Phys.* **2018**, *20*, 22197–22202.

(40) Foerster, B.; Spata, V. A.; Carter, E. A.; Sönnichsen, C.; Link, S. Plasmon Damping Depends on the Chemical Nature of the Nanoparticle Interface. *Sci. Adv.* **2019**, *5*, No. eaav0704.

(41) Walker, D. A.; Leitsch, E. K.; Nap, R. J.; Szeleifer, I.; Grzybowski, B. A. Geometric Curvature Controls the Chemical Patchiness and Self-Assembly of Nanoparticles. *Nat. Nanotechnol.* **2013**, *8*, 676–681.

(42) Wu, B.; Liu, D.; Mubeen, S.; Chuong, T. T.; Moskovits, M.; Stucky, G. D. Anisotropic Growth of TiO<sub>2</sub> onto Gold Nanorods for Plasmon-Enhanced Hydrogen Production from Water Reduction. *J. Am. Chem. Soc.* **2016**, *138*, 1114–1117.